



HAL
open science

Real-time detection and discrimination of radioactive gas mixtures using nanoporous inorganic scintillators

Raphael Marie-Luce, Pavlo Mai, Frederic Lerouge, Yannis Cheref, Sylvie Pierre, Benoit Sabot, Frederic Chaput, Christophe Dujardin

► **To cite this version:**

Raphael Marie-Luce, Pavlo Mai, Frederic Lerouge, Yannis Cheref, Sylvie Pierre, et al.. Real-time detection and discrimination of radioactive gas mixtures using nanoporous inorganic scintillators. Nature Photonics, 2024, 18 (10), pp.1037-1043. 10.1038/s41566-024-01507-x . hal-04732352

HAL Id: hal-04732352

<https://hal.science/hal-04732352v1>

Submitted on 14 Oct 2024

HAL is a multi-disciplinary open access archive for the deposit and dissemination of scientific research documents, whether they are published or not. The documents may come from teaching and research institutions in France or abroad, or from public or private research centers.

L'archive ouverte pluridisciplinaire **HAL**, est destinée au dépôt et à la diffusion de documents scientifiques de niveau recherche, publiés ou non, émanant des établissements d'enseignement et de recherche français ou étrangers, des laboratoires publics ou privés.



Distributed under a Creative Commons Attribution 4.0 International License






Real-time detection and discrimination of radioactive gas mixtures using nanoporous inorganic scintillators

Received: 14 March 2024

Accepted: 17 July 2024

Published online: 2 September 2024


 Check for updates

Raphael Marie-Luce^{1,5}, Pavlo Mai^{2,5}, Frederic Lerouge¹, Yannis Cheref^{1,2}, Sylvie Pierre³, Benoit Sabot³  , Frederic Chaput¹   & Christophe Dujardin^{2,4}  

The nuclear industry's expansion to encompass carbon-free electricity generation from small modular reactors and nuclear fuel reprocessing necessitates enhanced detection and monitoring of pure beta-emitting radioactive elements such as ^3H and ^{85}Kr ; this endeavour is crucial for nuclear safety authorities tasked with environmental monitoring. However, the short range of electrons emitted by these gases makes detection challenging. Current methods, such as ionization chambers and liquid scintillation, do not offer at the same time good sensitivity, real-time analysis and ease of implementation. We demonstrate an approach using a gas–solid mixture to overcome these limitations. We synthesized a transparent and scintillating nanoporous material, an aerogel of $\text{Y}_3\text{Al}_5\text{O}_{12}:\text{Ce}^{4+}$, and achieved real-time detection with an efficiency of 96% for ^{85}Kr and 18% for ^3H . The method reaches a sensitivity below 100 mBq per cm^3 over 100 s measurement time. We are able to measure simultaneously as mixtures containing both ^3H and ^{85}Kr a capability not possible previously. Our results demonstrate a compact and robust detection system for inline measurement of strategic radioactive gases. This combination of concept and method enhances nuclear power plant management and contributes to environmental safeguarding. Beyond the detection issues, this concept opens a wide field of new methods for radionuclide metrology.

Unstable radionuclides, which exist as natural elements or are produced by human activities, naturally emit ionizing radiations. The efficient detection of ionizing radiations is crucial across societal sectors, such as healthcare, security, energy and nuclear waste management. In the case of radionuclides that decay directly to the ground state in the atmosphere, it is necessary to detect the β or α radiation directly, which is very challenging owing to their short mean free path in air at normal pressure. The efficient detection of these radionuclides is,

in particular, critical for nuclear activities such as radioprotection and risk evaluation, the use of radioactive gas tracers in geosciences or astrophysics and the Comprehensive Nuclear-Test-Ban Treaty Organization (CTBTO), all of which requires a metrological level^{1–8}. As a result, detecting pure β -emitting radionuclides, particularly in the gaseous phase, poses an important challenge. Among the common pure β -emitting radionuclides, tritium (^3H) is one of the most difficult to measure⁹. It is due to its status as a low-energy β emitter (maximum

¹Laboratoire de Chimie, Ecole Normale Supérieure de Lyon, Université Claude Bernard Lyon 1, UMR 5182 ENS-CNRS-UCBL, Lyon, France. ²Université Claude Bernard Lyon 1, CNRS, ILM UMR 5306, Villeurbanne, France. ³Université Paris-Saclay, CEA, LIST, Laboratoire National Henri Becquerel, Palaiseau, France. ⁴Institut Universitaire de France (IUF), Paris, France. ⁵These authors contributed equally: Raphael Marie-Luce, Pavlo Mai.  e-mail: benoit.sabot@cea.fr; frederic.chaput@univ-lyon1.fr; christophe.dujardin@univ-lyon1.fr

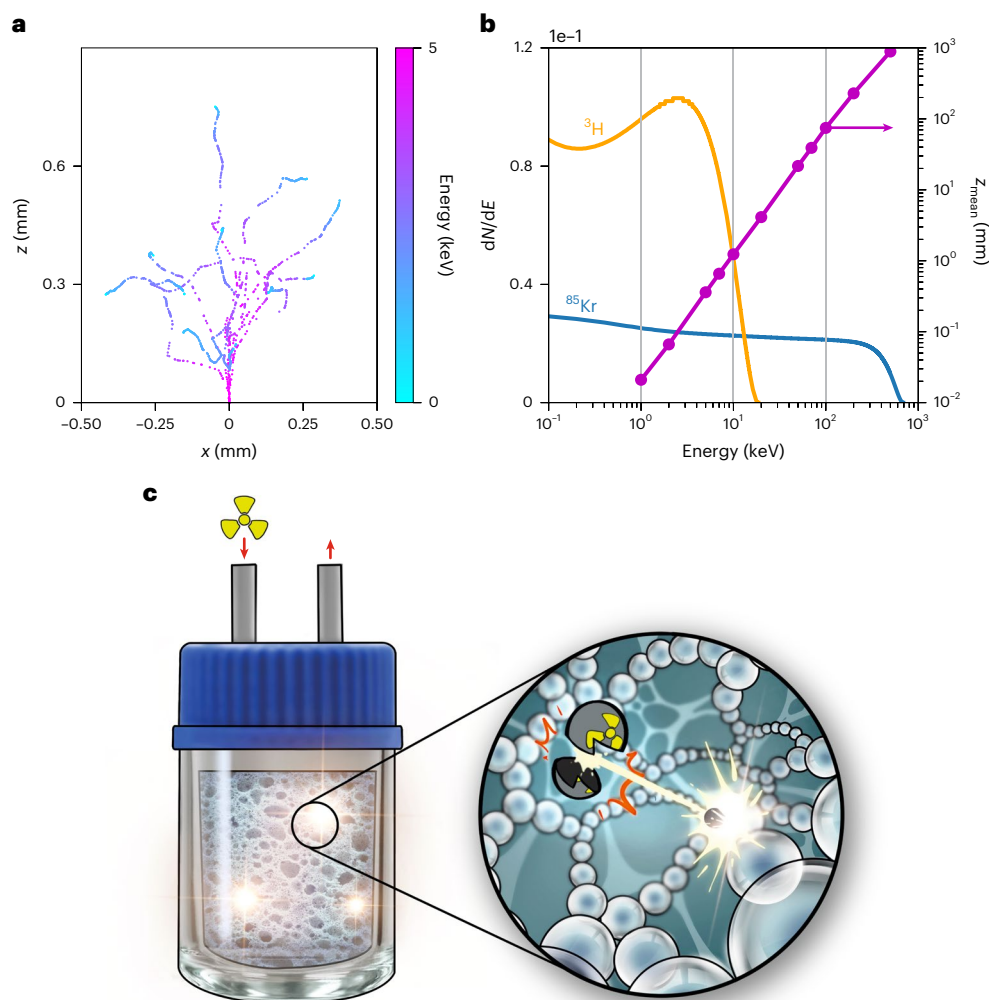


Fig. 1 | Electron trajectories and mean free paths in air for various representative initial energies. **a**, Monte Carlo simulation of 10 electron trajectories in air with an initial energy of 5 keV along the z -axis. The 2D map corresponds to the projection in the xz -plane. The remaining energy along the trajectory is indicated by the colour. **b**, Energy distribution of emitted electrons for ^3H and ^{85}Kr . For clarity, dN/dE has been multiplied by 10 for ^{85}Kr . The dashed

grey lines indicate the energies of 5 keV and 100 keV. Right axis (purple): mean value Z_{mean} of the maximum z value reached by the electrons in air, as a function of the initial energy. **c**, Schematic description of the nanoporous scintillating sponge in the vial. The radioactive gas, after being injected, diffuses inside the open porosity of the aerogel. Each electron interaction with the nanostructured material generates a flash of light.

energy $E_{\text{max}} = 18.6$ keV and average energy $E_{\text{av}} = 5.7$ keV)¹⁰. However, it is crucial to monitor ^3H because it is often involved in various nuclear activities, whether during mandatory controls by nuclear authorities, during the dismantling of nuclear power plants or during studies on the development of fusion. Another crucial anthropomorphic radionuclide is ^{85}Kr ($E_{\text{max}} = 687$ keV, $E_{\text{av}} = 251$ keV), which is a fission product generated at a very high concentration in the atmosphere during nuclear power plant operation and nuclear fuel reprocessing (6,300 TBq per year per GWe)¹¹. Normally, the detection of radioactive gases is possible but requires sampling and laboratory processing, particularly for ^3H using a bubbler and liquid scintillation. In this study, we present a method capable of directly detecting, inline, without destructive or polluting methods, gases such as low-energy pure beta emitters like ^3H .

Unlike X and γ emitters, low-energy β particles cannot be efficiently detected at a distance larger than tens of micrometres from a source. To illustrate this, using PENELOPE software¹², simulated trajectories of 5 keV electrons in air are presented in Fig. 1a. For almost all pure β emitters, the β emissions appear as a spectrum whose shape and distribution depend on the radionuclide¹³. Figure 1b shows the

energy spectra of electrons emitted during the decay of the radionuclides of interest, ^3H and ^{85}Kr , calculated with BetaShape 2.2 (ref. 14). The challenge of gas phase detection extends beyond just ^3H , to include other elements, but with ^3H , being one of the most difficult to detect. The particle's type and energy significantly influence the mean maximum distance travelled. In the case of β , the distance can range from a few micrometres to several tens of centimetres in air (Fig. 1b). Consequently, low-energy β cannot be detected at distances greater than a hundred micrometres. Moreover, these electrons deposit their energy as they travel through the air, resulting in rapid energy loss. This suggests that the highest detection efficiency is obtained when the radionuclide is incorporated in the sensing part of the detector, which is applied with different gas radionuclides in ionization chambers (gas–gas mixing) and for liquid solution in the liquid scintillation counting technique (gas–liquid mixing)¹⁵.

In gas-counting chambers, the radioactive gas is mixed with a counting gas (such as propane or argon-methane) and direct ionization is observed in the proportional counter mode. This technique is used in metrology for primary standardization of activity concentrations down to 200 Bq cm^{-3} (ref. 16). Ionization chambers are the most

sensitive type of counting device owing to their large volume. Among the various products, the largest one, with a volume of 8 L, is reported to initiate the detection of ^3H at a concentration of 5 kBq m^{-3} with an integration time of 90 s (ref. 17). Liquid scintillation counting technique is the standard technique for ^3H but cannot be performed inline.

Liquid scintillation is used in conjunction with a bubbler to capture ^3H present in the air with a certain transfer efficiency, estimated at 95% in the case of current commercial devices¹⁸. The bubbler aims either to retain water molecules charged with ^3H or to enable an isotopic exchange between the gaseous ^3H and water. This exchange is not possible with ^{85}Kr . In addition, ^{85}Kr 's solubility in a liquid scintillator is relatively low, making direct bubbling inefficient¹⁹. The only currently available technology for ^{85}Kr detection is the previously mentioned gas-counting technique. The overall cycle duration for one measurement takes approximately 1 week. In addition, after the measurements, the liquid scintillation mixed with water and ^3H becomes an organic radioactive waste that cannot be reused. In summary, neither gas–gas mixing nor gas–liquid mixing techniques can meet all the requirements for efficient and real-time detection of ^3H , ^{85}Kr and other pure β emitters. These methods also fail to meet additional requirements, such as being non-polluting during usage, easy to deploy and simple to clean. We hereby introduce the concept of gas–solid mixing to design an efficient detector, wherein the radioactive gas is introduced into a highly porous transparent inorganic scintillator. This novel approach, akin to a ‘scintillating sponge’, aims to produce a solid-state-based sensor that combines real-time read-out, high sensitivity in detecting pure β radioactive emitters (including ^3H), reusability, compactness and even cost-effectiveness. In brief, a micro-/nanoporous aerogel absorbs or facilitates the diffusion of the radioactive gas. Since this porous material is scintillating, the electron resulting from a radionuclide decay interacts over short distances with the scintillating material within a solid angle of 4π steradians (as sketched in Fig. 1c). To minimize light scattering within the porous architecture, it is imperative to mitigate Mie scattering until it falls below the Rayleigh scattering threshold, thus necessitating particle sizes smaller than $\lambda/10$. As a consequence, contrary to the powder-like metal–organic frameworks tested in^{20,21}, the nanoporosity ensures the material transparency over the whole material and allows the extraction of the light signal, which can be detected with double and/or triple coincidence techniques. In principle, a large specific area within a confined volume enables highly efficient detection of low-energy electrons such as those emitted by ^3H .

The study presents the results with a reference measuring device for liquid scintillation metrology^{22,23}. To fulfill the required scintillation criteria, it is crucial to attain the highest possible scintillation efficiency (at least >20 photons per keV) and the shortest scintillation decay time ($< a \text{ few } 100 \text{ ns}$), facilitating the use of the narrowest possible coincidence time window. In addition to achieving scintillation performance, which can be adequately met by several other compositions ($\text{Y}_2\text{SiO}_5\text{:Ce}^{3+}$, $\text{CeBr}_3\text{:...}$), it is also essential to ensure the preparation of large, transparent aerogels with excellent chemical stability against humidity and radiation, as well as high radiopurity. Lu-based compounds, therefore, cannot be considered. $\text{Y}_3\text{Al}_5\text{O}_{12}$ doped with cerium ions (YAG:Ce) satisfies these requirements. This well-known compound exhibits a fast allowed electric dipole transition $d-f$ of Ce^{3+} (about 70 ns to 90 ns depending on the producer and the excitation conditions) and efficient emission under photoexcitation or ionizing radiation^{24–26}.

Results

Aerogel preparation

By controlled destabilization of the YAG:Ce colloidal suspensions prepared by a solvothermal approach (particle size centred around 4.3 nm), monolithic gels were prepared²⁷. To achieve this, a water-miscible solvent mixture (ethanol/1,4-dioxane) of low dielectric constant was added to the concentrated colloid. Gelation then took place within a few hours,

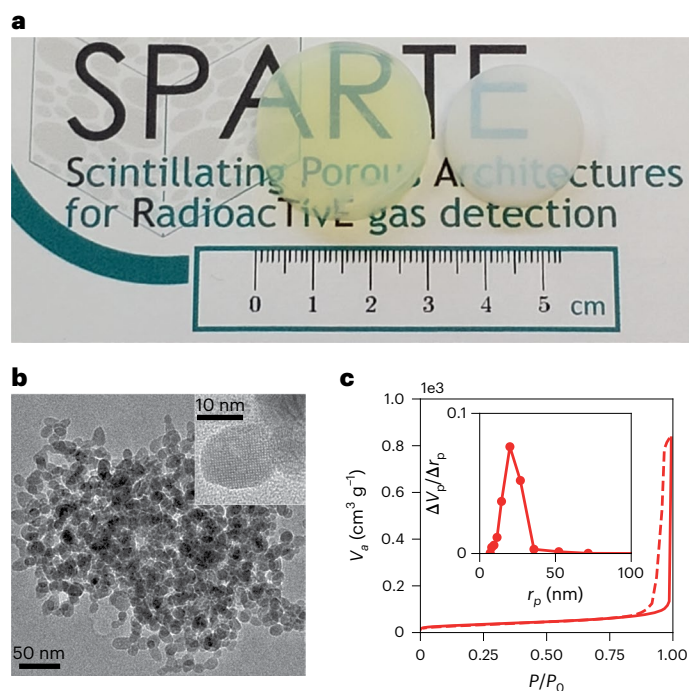


Fig. 2 | One typical studied porous scintillator assembly and its porosity property. **a**, Picture of aerogels before and after heat treatment at 750°C in air (white sample on the right). **b**, Transmission electron microscopy image of the YAG:Ce nanoparticles after thermal treatment at 750°C . **c**, Nitrogen adsorption and desorption isotherms (adsorption (red full), desorption (red dashed)). Inset (red scatter): pore radius distribution of the thermal annealed aerogel ($\text{cm}^3 \text{ nm}^{-1}$).

leading to transparent gels. To improve their mechanical properties, the gels were aged at room temperature for 24 h and then at 40°C for 48 h. The resulting gel is highly transparent, with a yellow colour characteristic of cerium absorption in the 3+ state ($4f-5d$ transitions).

Transparent or slightly opalescent aerogels were obtained after supercritical CO_2 drying of the gels (Fig. 2a). To optimize the optical and scintillation properties of the aerogels, high-temperature treatment under air was necessary (750°C , 1 h). This treatment leads to a well-crystallized nanoparticle with a diameter between 10 nm and 20 nm. Treatment at a higher temperature resulted in lower transmission in the visible range, which is detrimental to the intended application. The aerogels thus prepared were in the form of 24-mm-diameter, 10-mm-thick disks. Three of them were introduced into a standard 18.1 cm^3 liquid scintillation vial. The total volume of the aerogel was 16.5 cm^3 . The aerogel density was 0.36 g cm^{-3} . For comparison, the density of the YAG single crystal is 4.56 g cm^{-3} . Aerogel porosity was assessed by transmission electron microscopy and tomography (Fig. 2b and Supplementary Video 1) as well as by the Brunauer–Emmett–Teller (BET) method, leading to a specific area of $118 \text{ m}^2 \text{ g}^{-1}$ and pore size distribution peaking at 25 nm (Fig. 2c). The untreated aerogels are yellow, while air-treated ones turn white. This reflects the change of the cerium oxidation state from 3+ to 4+. In general, the presence of Ce^{4+} ions is detrimental to photoluminescence, which requires the optical absorption from the Ce^{3+} ion. The situation is very different, however, in the case of excitation by ionizing radiation. In this case, the cerium is excited by sequential capture of holes and electrons involving Ce^{4+} (ref. 28). Ce^{4+} bypasses the hole capture and is in this case an excellent active centre for YAG:Ce scintillation.

Scintillation of the aerogel

The spectral and time dependence of the X-ray-induced emission of the YAG:Ce⁴⁺ aerogel is presented in Fig. 3a. Because the primary interaction between the X-ray photon and the materials generates a hot electron,

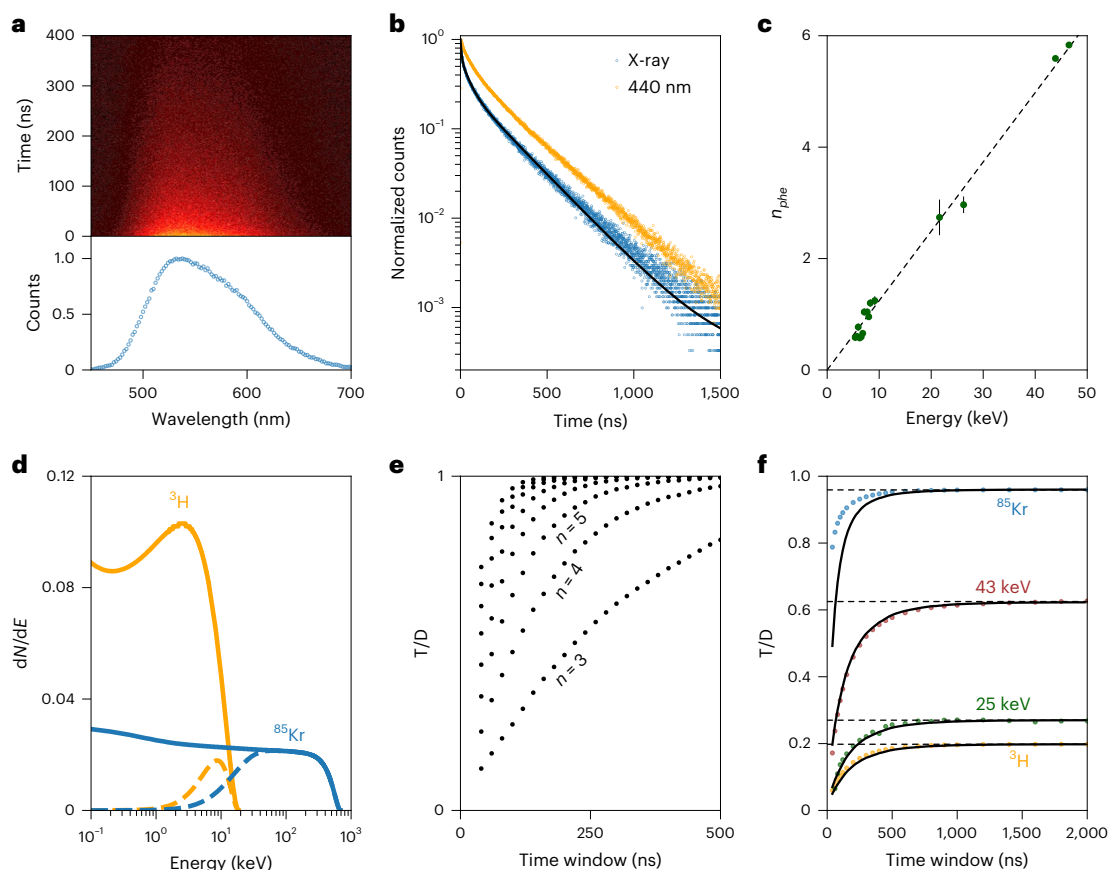


Fig. 3 | Scintillation properties of the YAG:Ce⁴⁺ aerogel. **a**, Top: 2D map (wavelength/time) radioluminescence of the YAG:Ce aerogel annealed in air at 750 °C. Bottom: radioluminescence spectra without time selection (blue open circles). **b**, Luminescence decay time under X-ray excitation (blue) and 440 nm excitation (orange) and curve fitting with three exponential functions (black). **c**, Experimental data (green scatterers) for electron excitation using the Compton electron and the photoelectron from the K-edge interaction of cerium (25 keV) and yttrium (43 keV). The error bars correspond to the absolute standard uncertainty evaluated for each measurement point following the guide for expressing uncertainties³⁴. The linear fit (black dashed line) leads to the

calibration curve³². **d**, Full line: energy distribution of electrons emitted for ³H and ⁸⁵Kr (as in Fig. 1b). Dashed line: corresponding calculated energy distribution of detected electrons based on the estimated number of double coincidences. **e**, Simulations of the expected evolution of T/D with the coincidence time window in the case of strictly n photons detected per scintillation event. **f**, Coloured circles: experimental evolution of T/D with the coincidence time window for monochromatic electrons at energies of 25 keV (green) and 43 keV (red), and for the radionuclides ³H (orange) and ⁸⁵Kr (blue). The black lines are the simulated T/D based on a Poissonian distribution of the number of photons detected, using the simulated data from **e**.

such an experiment is representative of a β interaction with the aerogels. The scintillation emission corresponds to the well-known broad spectral band centred at 550 nm similar to what has been observed in the case of powders and crystals²⁴. The temporal response under X-ray excitation is complex with 3 exponential components (217 ns (80.2%), 86.3 ns (17.3%) and 5.4 ns (2.4%); Fig. 3b). As shown by the photoluminescence decay time of samples treated under H₂ at 400 °C during 1 h and excited at 440 nm (orange curve in Fig. 3b), the main component corresponds to the radiative $5d-4f$ recombination of cerium. The observed lifetime is significantly extended compared with the crystal (88 ns)²⁶. This effect is related to the effective refractive index of the very sparse medium ($d = 0.36 \text{ g cm}^{-3}$ compared with $d = 4.56 \text{ g cm}^{-3}$ for the crystal), which strongly influences the radiative lifetime owing to Fermi's golden rule²⁹⁻³¹. The faster components observed in both decay curves correspond to extinction phenomena often observed, owing to quenching defects on the surface on doped insulating nanocrystals.

In liquid scintillation radionuclide metrology, the vial is surrounded by three photomultiplier (PMT) tubes with single photon counting capability. Using a defined time coincidence window, the number of double coincidences (D) is used to rule out noise counts and determine the activity. It has also been demonstrated that the ratio between the number of triple coincidences T to D is representative of

the average number of photons emitted and detected per event n_{phe} (known as the triple-to-double coincidence ratio (TDCR) technique²³). This technique is used to obtain the detection efficiency of the system while a radionuclide is placed in the liquid scintillator. We recently showed that this technique can also be applied as a method for scintillation characterization using an external monochromatic radioactive source and called Compton-TDCR³². We have measured the YAG:Ce⁴⁺ aerogel using an ²⁴¹Am source emitting γ -rays at 59.54 keV.

As a result, Fig. 3c indicates a good linearity of the scintillation response for electrons in the range from 5 keV to 50 keV, which corresponds to part of our range of interest for the detection of radioactive gases. The dashed line corresponds to a linear fit with a slope of 0.124 photoelectrons per keV. By extrapolating this curve to higher energies up to 600 keV, we deduce an estimate of the probability of obtaining a double coincidence as a function of the electron energy. By combining this probability with the energy spectra of the radionuclides presented in Fig. 1b, the detection efficiency of these radionuclides can be calculated as 96.3% for ⁸⁵Kr and 17.6% for ³H. This estimation is based on the assumption that all electrons interact with the solid material in the event of gas exposure and that energy deposition in the air within the pores is negligible. As expected, the loss of detection efficiency is greater in the low-energy part of the spectrum (Fig. 3d).

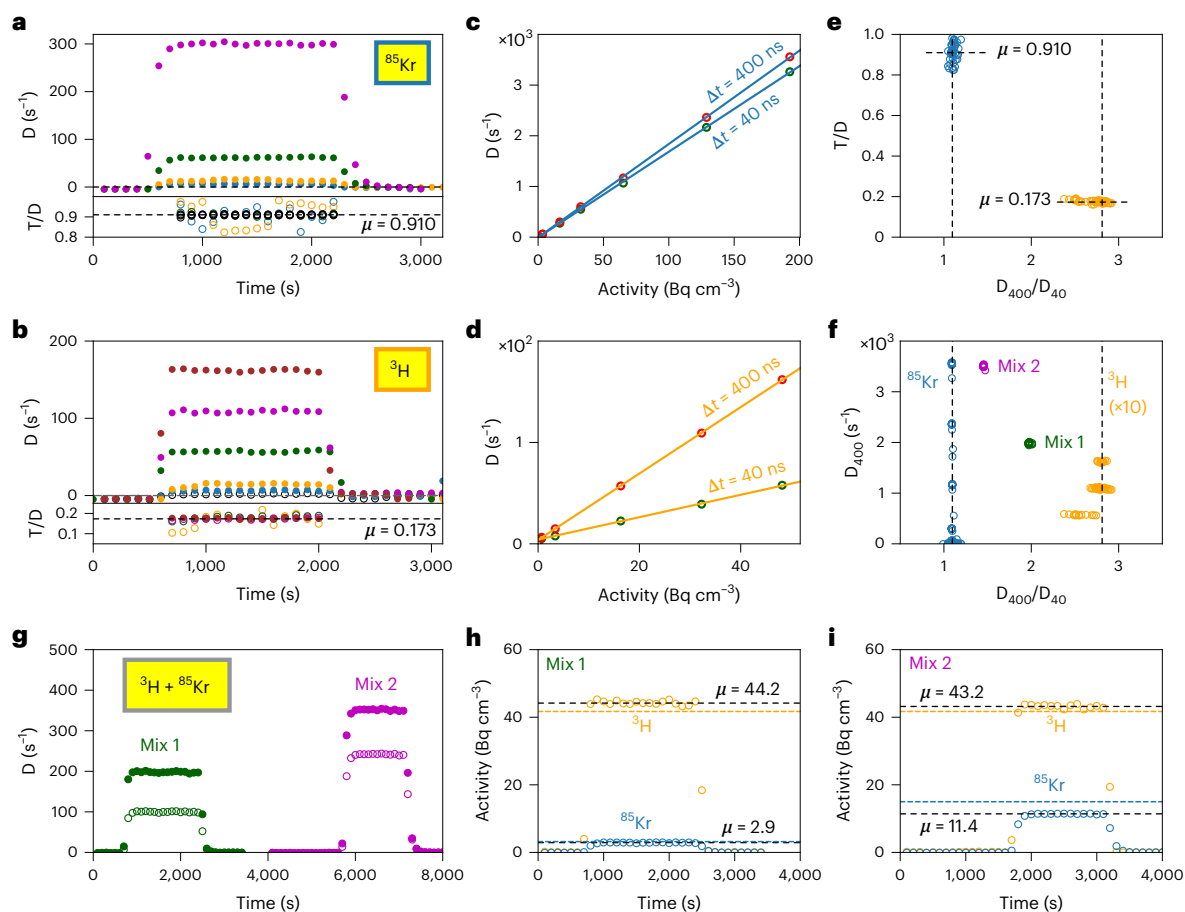


Fig. 4 | Inline detection evaluation of the nanoporous scintillator under ^3H and ^{85}Kr exposures. **a**, Evolution of the double coincidences (D) and the T/D coincidence ratio for several activities of ^{85}Kr (blue, 0.097 Bq cm^{-3} ; yellow, 0.668 Bq cm^{-3} ; green, 3.54 Bq cm^{-3} ; pink, 16.61 Bq cm^{-3}); higher measured activities up to 192.4 Bq cm^{-3} are not represented in the top panel. In the bottom panel, T/D for activities of 65.1 Bq cm^{-3} , 128.8 Bq cm^{-3} and 192.4 Bq cm^{-3} are represented as open black circles. **b**, Evolution of the double coincidences (D) and the T/D coincidence ratio for several activities of ^3H in the vial (open, 0.077 Bq cm^{-3} ; blue, 0.70 Bq cm^{-3} ; yellow, 3.38 Bq cm^{-3} ; green, 16.30 Bq cm^{-3} ; purple, 32.27 Bq cm^{-3} ; brown, 48.18 Bq cm^{-3}). In the bottom panel, T/D for activities of 32.25 Bq cm^{-3} and 42.12 Bq cm^{-3} are represented as open black circles. **c**, D values as a function of the activity per cm^3 of ^{85}Kr for 40 ns (green circles) and 400 ns (red circles) coincidence time windows. The blue curves correspond to linear fits. **d**, D values as a function of the ^3H activity per cm^3 for 40 ns (green circles) and

400 ns (red circles) coincidence time windows. The orange curves correspond to linear fits. **e**, T/D measured with a coincidence time window of 400 ns as a function of the ratio D_{400}/D_{40} . D_{40} (resp. D_{400}) is the number of double coincidences measured in the coincidence time windows of 40 ns (resp. 400 ns). Blue circles (resp. orange) correspond to ^{85}Kr (resp. ^3H). **f**, 2D plot of D_{400} versus D_{400}/D_{40} allowing to clearly identify ^{85}Kr (blue circles) and ^3H (orange circles). Purple and green circles correspond to the analysis of the gas mixtures mix 1 and mix 2. **g**, Evolution of the double coincidences D_{40} (open circles) and D_{400} (full circles) for the 2 gas mixtures mix 1 (green) and mix 2 (purple). **h**, **i**, Reconstruction, based on **g**, of the separated contributions of the two gases for both mix 1 (**h**) and mix 2 (**i**), which allows the deduction of the activity per cm^3 of each gas in each mixture (μ in Bq cm^{-3}). The black dashed line is the average deduced value, and the coloured dashed lines are the activities in the vial.

In addition, we can also examine the temporal properties of the aerogel. The X-ray-induced decay-time measurement represents the statistics of emission when the time stamp of the excitation is known. When measuring D or T , the arrival of the first photon detected is not predictable. Nevertheless, the X-ray decay curve allows us to simulate the time difference distribution between the first two and three photons (D resp. T), which depends on the number of detected photons (Supplementary Fig. 1). Figure 3e represents then the simulated evolution of T/D as a function of the coincidence time window when strictly 3, 4, 5... photons are emitted and detected for each event. Measurements of T/D as a function of the coincidence time window for electrons of 25 keV and 43 keV are presented Fig. 3f (green and red circles). That demonstrates that T/D values increase more slowly for small numbers of emitted photons corresponding to a small amount of deposited energy. Considering a Poissonian distribution of the number of photons per event, the simulated curve can clearly reproduce the experimental data. The same procedure was applied when the aerogel was exposed to ^3H and

^{85}Kr (yellow and blue points in Fig. 3f). While the ^3H curve could be fitted, the ^{85}Kr could not. Like ^3H , ^{85}Kr is non-monochromatic but has a much broader electron energy spectrum, extending from 0 keV to 687 keV. The high-energy electrons contribute to the fast rise, while the low-energy electrons contribute to the decrease of the average number of photons emitted per event, and hence the T/D . This key result highlights a clear interconnection between the time response and the energy deposited in the aerogel, offering a spectroscopic capability of the detector as demonstrated in the next paragraph. To obtain a sensitive dependence of the ratio with the mean number of detected photons (timing-based spectroscopy), the scintillation decay time has to be between 20 ns and 400 ns. In this respect, YAG:Ce^{4+} perfectly meets this additional constraint.

Radioactive gas detection with aerogel

The dedicated radioactive gas measurement set-up described in the Methods section enables us to expose the scintillating aerogel with

activity concentrations of ^3H and ^{85}Kr directly from primary standard measurement and dilution. A scintillation event is measured for each detected double coincidence within two selected coincidence time windows (named Δt) of 40 ns and 400 ns with our reference electronics³³. D and T are both measured during 100 s, including a correction for accidental coincidences, and the average T/D gives the average scintillation yield per event. Activities from about 0.07 Bq per cm^3 up to several kBq per cm^3 were injected in the porous scintillator and corresponding TDCR measurements performed with a coincidence window of 400 ns are presented in Fig. 4a,b for ^{85}Kr and ^3H (top part). The radioactive gas injection and removal can clearly be identified with the rapid increase and drop of D, the time response being faster than our 100 s counting rate integration. The average value of D when the radioactive element has diffused in the aerogel can be plotted as a function of the activity. These calibration curves are presented for ^{85}Kr and ^3H with 40 ns and 400 ns coincidence time windows and show a linear behaviour from 0.05 Bq cm^{-3} to 50 Bq cm^{-3} for ^3H and 200 kBq cm^{-3} for ^{85}Kr (Fig. 4c,d). Considering the volume of the vial (18.1 cm^3), the slopes of the calibration curves allow us to estimate a detection efficiency close to 100% for ^{85}Kr and 18.1% for ^3H . These values are very consistent with the predicted efficiencies of 96.3% and 17.3% presented in Fig. 3f with the Compton-TDCR method. This confirms the hypothesis that the energy deposited in the air contained in the pores along the electron path is negligible. In other words, this detector geometry does not entail significant energy losses.

Analysis of gas mixtures

During exposure, T/D is measured and, as expected, does not depend on the activity (bottom of Fig. 4a,b). The obtained T/D values lead to an average $\mu = 0.910$ for ^{85}Kr and $\mu = 0.173$ for ^3H . The significant difference of T/D values corresponds to the difference of the mean number of detected photons per event for the two radionuclides, reflecting their electron energy spectrum difference. T/D is also correlated to the ratio between the D values measured with time windows of 40 ns and 400 ns. In brief, when the number of detected photons per event is high, the D measured at $\Delta t = 40$ ns (D_{40}) is almost similar to D measured at $\Delta t = 400$ ns (D_{400}), since the probability to detect two photons within 40 ns is already high. Both measurements, T/D and D_{400}/D_{40} , provide insight on the electron mean energy of the radionuclides and can be used for radionuclide identification. This is demonstrated in Fig. 4e that shows T/D as a function of the D_{400}/D_{40} ratio for the two gases measured. One clearly distinguishes two clouds of points that are very localized, in blue for ^{85}Kr , and in yellow for ^3H . This graph encompasses all the measurement points, regardless of the injected activity. This presentation offers the capability of identifying the radionuclides. Furthermore, Fig. 4e represents D_{400} , indicating the activity, as a function of the D_{400}/D_{40} ratio. In a similar way, events from ^{85}Kr appear on a vertical line at D_{400}/D_{40} values close to 1 while events from ^3H appear on a vertical line around 2.8. This measurement map thus provides a dual indication: the nature of the gas and its activity in the measurement system. Note that, in this second case, a sensor with only two PMTs is sufficient to obtain this analysis, which is therefore compact and easily deployable. Moreover, this outcome allows us to propose a new concept to analyse krypton- ^3H mixtures that we tested with two different mixtures, labelled mix 1 and mix 2, containing respectively 3.2 Bq cm^{-3} of ^{85}Kr + 41.7 Bq cm^{-3} of ^3H and 15.0 Bq cm^{-3} of ^{85}Kr + 41.7 Bq cm^{-3} of ^3H (Fig. 4g). The standard uncertainties of activities are 3%. The values of D_{40} and D_{400} are presented in Fig. 4g for both mixtures and can be plotted in Fig. 4f where all the measurement points are considered. The two mixtures are clearly distinguishable, demonstrating the ability to identify purity of the gas as well as different mixtures. As seen in Fig. 4e, the ratio D_{400}/D_{40} for each pure gas is known. Considering that each measurement point corresponds to an average over 100 s, it is thus possible to extract the contribution to D_{400} for each gas. We then deduce the evolution of the respective activities of both gases while

they are mixed in the case of the two tested mixtures as presented in Fig. 4h,i. We found for mix 1 2.9 Bq cm^{-3} of ^{85}Kr and 44.2 Bq cm^{-3} of ^3H and for mix 2 11.4 Bq cm^{-3} of ^{85}Kr and 43.2 Bq cm^{-3} of ^3H , which are in very good agreement with the real activities injected in the porous scintillator.

Conclusion

This study demonstrates the feasibility of utilizing a nanostructured scintillator material with a large specific area to introduce a radically novel strategy for direct and real-time detection of radioactive gases. These measurements are crucial for the monitoring of nuclear activities across the globe and will benefit many future technologies in the field of nuclear energy. We have successfully developed a compact detector with real-time analysis capabilities (response time below 100 s), enabling the analysis of critical pure beta-emitting elements such as ^{85}Kr and ^3H with a sensitivity below 0.1 Bq per cm^3 . This represents an important breakthrough in the field of radioactivity measurement. ^{85}Kr and ^3H are two elements of the utmost importance in the field of nuclear energy production, since ^3H is an element naturally present in a power plant, and the abnormal presence of ^{85}Kr reveals a malfunction of the nuclear power plant. This method not only enables the inline measurement at high detection sensitivity of pure beta emitters using a non-polluting and non-destructive technique but also facilitates the inline separation of pure beta emitters through a technique combining both temporal and yield properties. This important achievement has never been accomplished before in the field of scintillation, as it was impossible with existing materials and conventional measurement techniques. To our knowledge, this is a major advancement in the field, which could greatly enhance the monitoring and control of current and future generations of nuclear reactors. Our innovative concept effectively addresses the growing demands of monitoring and controlling civil nuclear activities. This advancement paves the way for future developments in refining radioactivity metrology methods, enhancing standardization and exploring porous scintillating materials.

Online content

Any methods, additional references, Nature Portfolio reporting summaries, source data, extended data, supplementary information, acknowledgements, peer review information; details of author contributions and competing interests; and statements of data and code availability are available at <https://doi.org/10.1038/s41566-024-01507-x>.

References

1. Fukushima-Related Measurements by CTBTO (Comprehensive Nuclear-Test-Ban Treaty Organization, accessed 13 April 2011); <http://www.ctbto.org/press-centre/highlights/2011>
2. Bollhöfer, A. et al. Half a century of krypton-85 activity concentration measured in air over Central Europe: trends and relevance for dating young groundwater. *J. Environ. Radioact.* **205–206**, 7–16 (2019).
3. Cao, Y. et al. Long-term investigation of environmental radioactivity levels and public health around the Qinshan Nuclear Power Plant, China. *Sci. Rep.* **12**, 4945 (2022).
4. Aoyama, M. Long-term behavior of ^{137}Cs and ^3H activities from TEPCO Fukushima NPP1 accident in the coastal region off Fukushima, Japan. *J. Radioanal. Nucl. Chem.* **316**, 1243–1252 (2018).
5. Byun, J.-I. A multi-channel beta-gamma coincidence counting system using well-HPGe and plastic scintillation detectors for radioactive xenon measurements. *Nucl. Instrum. Methods Phys. Res. A* **949**, 162893 (2020).
6. Topin, S. et al. SPALAX new generation: new process design for a more efficient xenon production system for the CTBT noble gas network. *J. Environ. Radioact.* **149**, 43–50 (2015).

7. Topin, S. et al. 6 months of radionuclide detection in western Europe with the SPALAX—new generation system—part 1: metrological capabilities. *J. Environ. Radioact.* **225**, 106442 (2020).
8. Cagniant, A. et al. SPALAX NG: a breakthrough in radionuclide field measurement. *Appl. Radiat. Isot.* **134**, 461–465 (2018).
9. *TRANSVERSAL Actions for Tritium* (2022); <https://doi.org/10.3030/754586>
10. Chechev, V. *Table de Radionuclides, H-3* (CEA/LNE-LNHB, 2006); http://www.lnhb.fr/nuclides/H-3_tables.pdf
11. Yim, M.-S. *Generation of Nuclear Waste from Nuclear Power* 217–256 (Springer Netherlands, 2022).
12. NEA. *PENELOPE 2018: A Code System for Monte Carlo Simulation of Electron and Photon Transport: Workshop Proceedings, Barcelona, Spain, 28 January to 1 February 2019* (OECD Library, 2019).
13. Mougeot, X. Reliability of usual assumptions in the calculation of β and ν spectra. *Phys. Rev. C* **91**, 055504 (2015).
14. Mougeot, X. Atomic exchange correction in forbidden unique beta transitions. *Appl. Radiat. Isot.* **201**, 111018 (2023).
15. Knoll, G. F. *Radiation Detection and Measurement* 4th ed. (Wiley, 2010).
16. Unterweger, M., Johansson, L., Karam, L., Rodrigues, M. & Yunoki, A. Uncertainties in internal gas counting. *Metrologia* **52**, S156–S164 (2015).
17. *DT D - XPR80, Détecteur de tritium en ligne* (Mirion, accessed 12 January 2023); <https://www.mirion.com/fr/products/technologies/radiation-monitoring-systems/detectors-and-custom-channels/dt-d-xpr80-on-line-tritium-detector>
18. Analysis, M. P. *HT ionix – Barboteur tritium* (accessed 12 January 2023); <https://www.mirion.com/fr/products/technologies/radiation-monitoring-systems/tritium-measurement/tritium-samplers/ht-ionix-tritium-bubblers>
19. Hohorst, F. A. & Sherlock, M. A. *Partitioning of Krypton-85 in Liquid Scintillation Cocktail* Tech. Rep. (Lockheed Idaho Technologies Company, 1994).
20. Orfano, M. et al. Efficient radioactive gas detection by scintillating porous metal–organic frameworks. *Nat. Photon.* **17**, 672–678 (2023).
21. Mauree, S. et al. Detection of radioactive gas with scintillating MOFs. *Adv. Funct. Mater.* **33**, 2302877 (2023).
22. Sabot, B., Dutsov, C., Cassette, P. & Mitev, K. Performance of portable TDCR systems developed at LNE-LNHB. *Appl. Radiat. Isot.* **1034**, 166721 (2022).
23. Broda, R., Cassette, P. & Kossert, K. Radionuclide metrology using liquid scintillation counting. *Metrologia* **44**, S36 (2007).
24. Kvapil, J. et al. The luminescence efficiency of YAG:Ce phosphors. *Czech. J. Phys.* **30**, 185–192 (1980).
25. Zych, E., Brecher, C. & Glodo, J. Kinetics of cerium emission in a YAG:Ce single crystal: the role of traps. *J. Condens. Matter Phys.* **12**, 1947–1958 (2000).
26. Moszyński, M., Ludziejewski, T., Wolski, D., Klamra, W. & Norlin, L. Properties of the YAG:Ce scintillator. *Nucl. Instrum. Methods Phys. Res. A* **345**, 461–467 (1994).
27. Odziomek, M. et al. From nanoparticle assembly to monolithic aerogels of YAG, rare earth fluorides, and composites. *Chem. Mater.* **30**, 5460–5467 (2018).
28. Nikl, M. et al. Defect engineering in Ce-doped aluminum garnet single crystal scintillators. *Cryst. Growth Des.* **14**, 4827–4833 (2014).
29. Meltzer, R. S., Feofilov, S. P., Tissue, B. & Yuan, H. B. Dependence of fluorescence lifetimes of $\text{Y}_2\text{O}_3:\text{Eu}^{3+}$ nanoparticles on the surrounding medium. *Phys. Rev. B* **60**, R14012–R14015 (1999).
30. LeBihan, V. et al. Critical dimension where the macroscopic definition of refractive index can be applied at a nanometric scale. *Phys. Rev. B* **78**, 113405 (2008).
31. Bárta, J., Čuba, V., Pospíšil, M., Jarý, V. & Nikl, M. Radiation-induced preparation of pure and Ce-doped lutetium aluminium garnet and its luminescent properties. *J. Mater. Chem.* **22**, 16590 (2012).
32. Sabot, B. et al. A compact detector system for simultaneous measurements of the light yield non-linearity and timing properties of scintillators. *Sci. Rep.* **14**, 6960 (2024).
33. Jordanov, V., Cassette, P., Dutsov, C. & Mitev, K. Development and applications of a miniature TDCR acquisition system for in-situ radionuclide metrology. *Nucl. Instrum. Methods Phys. Res. A* **954**, 161202 (2020).
34. *Evaluation of Measurement Data—Guide to the Expression of Uncertainty in Measurement* (Working Group 1 of the Joint Committee for Guides in Metrology, 2008); <https://doi.org/10.59161/JCGM100-2008E>

Publisher's note Springer Nature remains neutral with regard to jurisdictional claims in published maps and institutional affiliations.

Open Access This article is licensed under a Creative Commons Attribution-NonCommercial-NoDerivatives 4.0 International License, which permits any non-commercial use, sharing, distribution and reproduction in any medium or format, as long as you give appropriate credit to the original author(s) and the source, provide a link to the Creative Commons licence, and indicate if you modified the licensed material. You do not have permission under this licence to share adapted material derived from this article or parts of it. The images or other third party material in this article are included in the article's Creative Commons licence, unless indicated otherwise in a credit line to the material. If material is not included in the article's Creative Commons licence and your intended use is not permitted by statutory regulation or exceeds the permitted use, you will need to obtain permission directly from the copyright holder. To view a copy of this licence, visit <http://creativecommons.org/licenses/by-nc-nd/4.0/>.

© The Author(s) 2024

Methods

Sample preparation

YAG:Ce nanoparticles were prepared by glycothermal synthesis (300 °C, 2 h) taking care to control the solvent composition (1,4-butanediol and diethylene glycol in a 17:3 ratio) and to dehydrate the commercial rare earth salts (yttrium and cerium acetates)³⁵. Distilled aluminium isopropoxide was used as the aluminium precursor. The nanoparticles were extracted from the reaction medium by successive precipitations with an acetone/diethyl ether mixture and centrifugations. As aerogel preparation requires several grams of nanocrystal, the synthesis method was scaled up to 40 g per batch in a 3 L reactor. The phase purity was checked by X-ray diffraction (XRD) (Supplementary Fig. 2) and energy-dispersive X-ray spectroscopy. Particle size distribution measured by dynamic light scattering resulted in a mean particle size of 4.3 nm with a standard deviation of 1.3 nm (Supplementary Fig. 3). The presence of acetate ligands on the particle surface was confirmed by infrared spectroscopy (Supplementary Fig. 4). These ligands were subsequently removed by acid washing. The purified bare nanocrystals were dispersed in water to prepare a colloidal solution with a high solid content (40% by weight). The particles exhibit a zeta potential greater than 40 mV in the acidic pH range (Supplementary Fig. 5).

Simulations

To accurately simulate the energy absorption of a beta emitter within a material or gas, we use the Monte Carlo PENELOPE 2018 code³⁶. This code is proficient in simulating the transport of lower-energy electrons, reaching down to approximately 250 eV within a material. It stands as the gold standard in terms of modelling low-energy electron transport, thanks to its highly detailed physical model. Notably, a valuable feature of this code is its ability to directly input the beta spectra emitted by a radionuclide, which is calculated using BetaShape 2.2 (ref. 13). Within the code, we define the material or gas based on its atomic composition and tailor its shape to suit our specific requirements.

To simulate the evolution of the T/D ratio as a function of the coincidence time window, a homemade Python programme using the Monte Carlo method was implemented. The scintillation decay measured under X excitation represents the probability law of photon emission following the excitation. Using this probability law, 10⁶ scintillation events were simulated to obtain photon arrival times per event. The distribution of the time difference between the first two photons for situations where the scintillation event produces strictly $m = 2, 3, 4, \dots$ photons can thus be constructed (Supplementary Fig. 1). Simulations have been performed with m up to $m = 50$. The distribution of the time difference between the first and third photons can likewise be reconstructed with $m = 3, 4, 5, \dots$. Considering a Poissonian distribution of the various m centred on a n_{average} value as a free parameter, the temporal evolution of T/D as a function of the coincidence time window can be fitted (Fig. 3f).

Experimental details for aerogel characterizations

The XRD pattern of cerium-doped YAG nanoparticles was measured using a Malvern Panalytical Empyrean X-ray diffractometer (Cu K α radiation at 0.154184 nm) equipped with a Ni filter and a PIXcel3D detector. The data were collected over a range of 10° to 70° (2 θ), with a scan speed of 0.5° min⁻¹ and a step width of 0.02° (Supplementary Fig. 2). Particle size and zeta potential of particles in aqueous suspension were determined by dynamic and electrophoretic light scattering using a Litesizer 500 (Anton Paar). In addition to the distribution of these variables, their variation as a function of pH was determined using an automated dosing system (867 pH Module, Metrohm) (Supplementary Figs. 3 and 5). Fourier transform infrared (FTIR) analysis of the samples was performed using a PerkinElmer Spectrum 100 FTIR spectrophotometer equipped with an attenuated total reflectance sample chamber (Supplementary Fig. 3). N₂ adsorption isotherms at 77 K were collected

up to 1 bar using a Belsorp-Max apparatus. The samples were prepared as follows: 50 mg of aerogel was degassed overnight at 120 °C under high vacuum (0.1 mbar), to remove adsorbed water. Low-temperature (77 K) nitrogen adsorption isotherms were fitted using the BET model, and surface areas were calculated in the range of 0.04 to 0.3 P/P₀. Pore size distributions were estimated according to the Dollimore and Heal model, relevant for mesoporous materials. TEM analyses were carried out using a JEOL JEM 2100F transmission electron microscope operating at 200 kV and equipped with a Gatan Ultrascan 1000 CCD camera and an Oxford X-Max 80 mm² EDS spectrometer. The TEM samples were prepared by depositing highly diluted nanoparticles on 300 mesh copper grids coated with an ultrathin carbon film.

Time-resolved emission spectra under X-ray excitation were obtained using a pulsed laser DeltaDiode-405L from Horiba emitting at 405 nm hitting the photocathode of an X-ray tube from Hamamatsu (N5084) set at 35 kV. Emitted light was collected using a monochromator from Andor (Kymera 193i) with a grating of 300 lines per mm. Detection is performed using a hybrid photomultiplier tube (HPM 100-40c) from Becker & Hickl GmbH. Time-resolved analysis is performed using a multichannel counter MCS6A from Fast ComTec (0.8 ns per channel). A custom software drives the monochromator and records the decay time for each wavelength. The reconstruction of the time-gated emission spectra as well as the wavelength resolved scintillation decay time are performed offline. For decay time measured under optical excitation, a DeltaDiode-440L from Horiba emitting at 440 nm replaced the X-ray source.

The TDCR method

The TDCR is widely used by national metrology institutes as a primary measurement technique for the standardization of pure beta emitters by liquid scintillation in radionuclide metrology²³. The principle of this technique involves determining the light yield of a liquid scintillator by minimizing the theoretical detection efficiency equation, which is based on Poisson distribution and the Birks model³⁷, using the experimental values of triple and double coincidences. The application of the method requires the use of a specialized counter with three PMTs and electronics that is able to record the triple (T) and double (AB, BC, AC) coincidence counting rates. A logical sum of the double coincidences (D) channel can be defined as the logical or of the three double channels. Under the assumption of three identical PMTs, for a given radionuclide pure beta emitter with emission spectra $S(E)$, the ratio of the detection efficiency in the T channel to that in the D channel is²³

$$\frac{\epsilon_T}{\epsilon_D} = \frac{\int_0^{E_{\max}} S(E)(1 - e^{-\bar{n}(E)/3})^3 dE}{\int_0^{E_{\max}} S(E) [3(1 - e^{-\bar{n}(E)/3})^2 - 2(1 - e^{-\bar{n}(E)/3})^3] dE}, \quad (1)$$

where \bar{n} is the average number of photons detected for effective energy E deposited in the cocktail and is the same parameter defined in equation (3):

$$\bar{n}(E) = \varphi L(E), \quad (2)$$

where φ is the free parameter and $L(E)$ is the Birks semi-empirical ionization quenching formula, which is the most widely used equation for describing the non-linearity of organic scintillators. This formula relates the light output of the scintillator, denoted as L , to the deposited energy E , and it is defined by

$$L(E) = \frac{1}{E} \int_0^E \frac{dE}{1 + kB(dE/dx)}. \quad (3)$$

For a large number of detected events, the ratio of the T to D coincidences tends towards the ratio of the detection efficiencies or

$T/D = \epsilon_T/\epsilon_D$. The free parameter φ can then be obtained by minimizing the squared difference between the two ratios. In the case of non-identical PMTs, a set of three equations must be used, including the relative efficiencies of the three PMTs. The equations are used to optimize the three free parameters of the system: $\varphi_A = \epsilon_A\varphi$, $\varphi_B = \epsilon_B\varphi$ and $\varphi_C = \epsilon_C\varphi$.

In this document, we utilize TDCR both as a scintillation yield indicator and as a novel approach to process the results when dealing with the demixing of mixed beta emitters measured with porous materials.

Radioactive gas exposure experiments

Exposure tests involving radioactive gases are conducted at the National Radioactivity Metrology Laboratory in France using the test bench described in Sabot et al.³⁸. This specialized set-up enables the controlled creation of radioactive gas atmospheres using primary standards of radioactive gas with high activity. In this study, we used predetermined quantities of various radioactive gases, creating dilutions in dry, filtered air, which ensured the absence of moisture and aerosols. These gas atmospheres, characterized by precisely known volume activities, were circulated through porous scintillator samples enclosed in glass vials. The exposure of the samples followed distinct experimental steps, as outlined below:

- background evaluation: circulation of clean air without additional radioactivity,
- introduction of either krypton (⁸⁵Kr), ³H or a mixture sample into the vial containing the scintillator circulation of radioactive gas at 0.7 l min⁻¹, and
- circulation of clean air through the device to eliminate the radioactive gas.

During these exposures, the light photons emitted by the scintillator were continuously and directly measured using reference detection instrumentation designed for the flow of radioactive gas. This instrumentation corresponds to a measurement device based on the TDCR method. In this case, we utilized the recently developed portable device from the laboratory²², renowned for its exceptional sensitivity and performance. During each exposure in the closed loop to a radioactive gas, the three PMTs record pulses with dedicated extendable dead-time electronics already validated at the metrology lab³³. Each measurement lasts for 100 s to monitor the evolution of coincidence counting (AB, BC, AC, T and D) for two coincidence window durations of 40 ns and 400 ns. Tracking D enables us to obtain the detection efficiency of the device as a function of the injected activity, and tracking T/D provides us with information regarding detection efficiency.

Data availability

The data that support the plots within this paper and the Supplementary Information are available in figshare data repository.

References

35. Odziomek, M., Chaput, F., Lerouge, F., Sitarz, M. & Parola, S. Highly luminescent YAG:Ce ultra-small nanocrystals, from stable dispersions to thin films. *J. Mater. Chem. C* **5**, 12561–12570 (2017).
36. Salvat, F., Fernández-Varea, J. M. & Sempau, J. *PENELOPE-2018: A Code System for Monte Carlo Simulation of Electron and Photon Transport*. Issy-les-Moulineaux, France: OECD/NEA Data Bank (2018); <http://www.nea.fr/lists/penelope.html>
37. Birks, J. B. *The Theory and Practice of Scintillation Counting* (Pergamon Press, 1964).
38. Sabot, B., Rodrigues, M. & Pierre, S. Experimental facility for the production of reference atmosphere of radioactive gases (Rn, Xe, Kr, and H isotopes). *Appl. Radiat. Isot.* **155**, 108934 (2020).

Acknowledgements

We acknowledge support from the European Community through grant number 899293, HORIZON 2020—SPARTE (all authors). We thank N. Blanchard for his proofreading.

Author contributions

R.M.-L., F.L., Y.C. and F.C. designed, synthesized and characterized the scintillating aerogel. P.M. and C.D. conceived and performed the photoluminescence and radioluminescence experiments. B.S., S.P., C.D. and P.M. designed, performed and analysed the gas detection experiments. C.D., F.C. and B.S. conceived the project and wrote the paper.

Competing interests

The authors declare no competing interests.

Additional information

Supplementary information The online version contains supplementary material available at <https://doi.org/10.1038/s41566-024-01507-x>.

Correspondence and requests for materials should be addressed to Benoit Sabot, Frederic Chaput or Christophe Dujardin.

Peer review information *Nature Photonics* thanks the anonymous reviewers for their contribution to the peer review of this work.

Reprints and permissions information is available at www.nature.com/reprints.